12-11-2020

Low-Temperature Crystal Structure and Mean-Field Modeling of ErxDy1−xAl2 Intermetallics

Yaroslav Mudryk
Ames Laboratory, slavkomk@ameslab.gov

Bruno P. Alho
Ames Laboratory and Universidade do Estado do Rio de Janeiro

Paula O. Ribeiro
Ames Laboratory and Universidade do Estado do Rio de Janeiro

Vitalij K. Pecharsky
Iowa State University and Ames Laboratory, vitkp@ameslab.gov

Low-Temperature Crystal Structure and Mean-Field Modeling of ErxDy1−xAl2 Intermetallics

Abstract

Low-temperature crystal structure of the $Er_xDy_{1-x}Al_2$ alloys with x = 0.45, 0.67, 0.90 was examined using temperature-dependent powder X-ray diffraction. The Er-rich sample, $Er_{0.9}Dy_{0.1}Al_2$, exhibits a rhombohedral distortion associated with the magnetic ordering that occurs around 20 K. The rhombohedral distortion is suppressed in $Er_{0.67}Dy_{0.33}Al_2$, while a weak low-temperature tetragonal distortion is observed in $Er_{0.45}Dy_{0.55}Al_2$. The mean-field theory supports the correlation between the type of structural distortion and the variable easy magnetization axis in $Er_xDy_{1-x}Al_2$ intermetallics.

Keywords

rare earths, intermetallic compounds, phase transformations, mean-field modeling

Disciplines

Engineering Physics | Metallurgy

metals

MDPI

Article

Low-Temperature Crystal Structure and Mean-Field Modeling of $Er_xDy_{1-x}Al_2$ Intermetallics

Yaroslav Mudryk [1,*], Bruno P. Alho [1,2], Paula O. Ribeiro [1,3] and Vitalij K. Pecharsky [1,4]

1 Ames Laboratory, U.S. Department of Energy, Iowa State University, Ames, IA 50011, USA; brunoalho@uerj.br (B.P.A.); paula.ribeiro@uerj.br (P.O.R.); vitkp@ameslab.gov (V.K.P.)
2 Instituto de Física Armando Dias Tavares, Universidade do Estado do Rio de Janeiro, Rio de Janeiro 20550-013, Brazil
3 Instituto de Aplicação Fernando Rodrigues da Silveira, Universidade do Estado do Rio de Janeiro, Rio de Janeiro 20261-232, Brazil
4 Department of Materials Science and Engineering, Iowa State University, Ames, IA 50011, USA
* Correspondence: slavkomk@ameslab.gov; Tel.: +1-515-294-2728

Received: 9 November 2020; Accepted: 7 December 2020; Published: 11 December 2020

Abstract: Low-temperature crystal structure of the $Er_xDy_{1-x}Al_2$ alloys with x = 0.45, 0.67, 0.90 was examined using temperature-dependent powder X-ray diffraction. The Er-rich sample, $Er_{0.9}Dy_{0.1}Al_2$, exhibits a rhombohedral distortion associated with the magnetic ordering that occurs around 20 K. The rhombohedral distortion is suppressed in $Er_{0.67}Dy_{0.33}Al_2$, while a weak low-temperature tetragonal distortion is observed in $Er_{0.45}Dy_{0.55}Al_2$. The mean-field theory supports the correlation between the type of structural distortion and the variable easy magnetization axis in $Er_xDy_{1-x}Al_2$ intermetallics.

Keywords: rare earths; intermetallic compounds; phase transformations; mean-field modeling

1. Introduction

The interactions between two or more elements containing 4*f* electrons is a fascinating topic [1–3] with potential practical importance for novel technologies such as magnetocaloric cooling [4–6]. The sheer number of known and yet to be discovered intermetallic compounds containing 4*f* elements is enormous, and this broad family becomes nearly infinite when considering the ability to partially substitute one lanthanide element with another. Further, intra rare earth substitutions involving twelve magnetic lanthanide ions (excluding non-magnetic Lu and La, as well as unstable Pm) lead to captivating basic science rooted in the steeply increased complexity of magnetic interactions. It is known that magnetic exchange between the localized, spatially separated 4*f* orbitals is mediated by the conduction electrons (Ruderman–Kittel–Kasuya–Yosida, RKKY-type interactions) [7–10]. In magnetic lanthanides with a non-zero orbital quantum number, L, the presence of spin-orbit coupling and site-dependent crystalline electric fields lead to the splitting of the 4*f* energy levels and their population by electrons creating unusually complex magnetic structures [10–14]. Further, the intimate coupling between magnetic and crystallographic sublattices often translates the magnetic complexity into crystallographic one (and vice versa) leading to a variety of magnetostructural phenomena [15–17]. Giant magnetostriction in ($Tb_{1-x}Dy_xFe_2$) [18,19] and giant room temperature magnetocaloric effect in ($Gd_5Si_2Ge_2$) [20,21] among others, take origin in the magnetoelastic coupling, signifying its practical and fundamental significance.

Among broadly known model systems routinely tapped to study magnetostructural phenomena is the family of intermetallic Laves phases that adopt $MgCu_2$-type crystal structure crystallizing in cubic space group $Fd\bar{3}m$; in particular compounds exhibiting strong magnetocrystalline anisotropy in

their magnetically ordered states [3,10,19,22–27]. The RM_2 Laves phase compounds, where R is a rare earth element and M is a *d*- or *p*-element, for example, Mn, Fe, Co, Ni or Al, show clear correlations between magnetic anisotropy and the type of crystallographic distortions that occur in parallel with magnetic ordering [10,28]. In such compounds, the easy magnetization axis (EMA) determines whether the material undergoes cubic to tetragonal (EMA <100>), rhombohedral (EMA <111>), or orthorhombic (EMA <110>) distortions. Consequently, many magnetic binary RM_2 compounds adopt low-temperature crystal structures related to their EMAs. In rare cases, e.g., in $HoCo_2$, a compound may exhibit more than one crystallographic transformation reflecting spin-reorientation transitions that change EMA [29].

The structural transitions become harder to predict and model in pseudobinary systems containing two rare earth elements whose corresponding binary parents adopt different EMAs in the magnetically ordered states, and, consequently, different low-temperature crystal structures. Here, additional complexities associated with intra-lanthanide substitutions, such as lattice disorder (e.g., when different rare-earth atoms randomly occupy the same atomic site), and exchange interactions between 4*f* orbitals of different elements modified by crystalline electric field splitting come into play, producing unexpected results. For example, a recent study of $Er_xDy_{1-x}Co_2$ compounds shows that at $x = 0.75$ the compound is mimicking the behavior of $HoCo_2$, including the presence of a second crystallographic transition [3]. However, earlier temperature-dependent X-ray powder diffraction study of the $Er_{0.75}Dy_{0.25}Al_2$ alloy [30], where behaviors similar to $Er_{0.75}Dy_{0.25}Co_2$ may be expected due to competition between Er and Dy ions showed no signs of any structural transformation below its Curie temperature, T_C, despite the first-order nature of spin reorientation transition observed below T_C clearly evidenced by heat capacity data.

Both $ErCo_2$ and $ErAl_2$ Laves phase compounds adopt <111> as EMA, and both undergo a rhombohedral distortion [24,26], while $DyCo_2$ and $DyAl_2$ are both reported to be tetragonal at low temperature [23,26]. In $Er_xDy_{1-x}Co_2$ the M element, Co, carries magnetic moment, and the onsets of magnetic ordering in the Co sublattice are responsible for the discontinuous volume changes observed during the first-order transitions in $DyCo_2$ and $ErCo_2$. The non-magnetic aluminum, on the other hand, does not bring itinerant magnetism to bear, and $Er_xDy_{1-x}Al_2$ compounds should, in principle, exhibit magnetostructural behavior that reflects fundamental interactions between the Er and Dy 4*f* orbitals. With this in mind, we performed a temperature-dependent crystallographic study of the $Er_xDy_{1-x}Al_2$ compounds with $x = 0.45$, 0.67, and 0.90 in order to understand how the interactions between two magnetic rare-earth sublattices influence the low-temperature crystallography. The physical behaviors (heat capacity and magnetization) of these materials are known and reported [31,32], yet data about their low-temperature crystal structures are lacking. In this work, we also use previously published X-ray powder diffraction data of $ErAl_2$, $Er_{0.75}Dy_{0.25}Al_2$, and $DyAl_2$ compounds [23,24,30] for comparison. Further, we use the mean-field theory tested earlier on similar R'R"Al_2 pseudobinary systems [33,34] to explain how the low-temperature crystallographic behavior evolves with a composition by modeling how the EMAs of Er and Dy sublattices change as functions of temperature (T) and of Er concentration (x).

2. Experimental

The samples used in this study were the same specimens that were prepared and thoroughly investigated in [32]. The samples are stable at ambient conditions and the sample surface retains metallic luster showing no visible traces of oxidation or corrosion after storage in a standard laboratory climate-controlled atmosphere for ~10 years. The samples were ground into fine powders, screened to eliminate particles greater than 25 μm, and mixed with GE varnish; the obtained paste was placed and solidified in a custom-made copper sample holder and the sample surface was polished flat. The temperature-dependent X-ray powder diffraction data were obtained on a Rigaku TTRAX rotating anode diffractometer (Rigaku, Japan) equipped with a continuous helium-flow cryostat and a superconducting magnet; the sample space is pumped down to 10^{-6} Torr to ensure temperature stability

of the measurements. A detailed description of the setup and the sample preparation procedure can be found elsewhere [35].

The powder X-ray diffraction (PXRD) patterns were collected in the temperature range between 5 K and room temperature in the absence of an applied magnetic field. The range of measured Bragg angles was $8° \leq 2\theta \leq 57°$ (Mo Kα radiation). The obtained PXRD patterns were analyzed using Rietveld refinement software Rietica [36] and FullProf [37,38].

3. Modeling

In order to theoretically investigate $Er_xDy_{1-x}Al_2$ we consider model Hamiltonians that include two main contributions for both Er and Dy rare earth sublattices, namely, exchange interactions and crystalline electric field splitting [34,39,40].

$$\mathcal{H}^{\mathrm{Er}} = -g^{\mathrm{Er}}\mu_B\left[x\lambda^{\mathrm{Er}}\vec{M}^{\mathrm{Er}} + x(1-x)\lambda^{\mathrm{ErDy}}\vec{M}^{\mathrm{Dy}}\right]\cdot\vec{J}^{\mathrm{Er}} + \mathcal{H}^{\mathrm{Er}}_{\mathrm{CEF}}, \quad (1)$$

$$\mathcal{H}^{\mathrm{Dy}} = -g^{\mathrm{Dy}}\mu_B\left[(1-x)\lambda^{\mathrm{Dy}}\vec{M}^{\mathrm{Dy}} + x(1-x)\lambda^{\mathrm{ErDy}}\vec{M}^{\mathrm{Tm}}\right]\cdot\vec{J}^{\mathrm{Dy}} + \mathcal{H}^{\mathrm{Dy}}_{\mathrm{CEF}}. \quad (2)$$

The first terms in (1) and (2) represent exchange interactions for a given concentration of x and $1 - x$ of Er and Dy, respectively. The g and J are the Landé factors ($g^{\mathrm{Er}} = \frac{6}{5}$ and $g^{\mathrm{Dy}} = \frac{4}{3}$) and total angular momentum quantum numbers ($J^{\mathrm{Er}} = J^{\mathrm{Dy}} = 15/2$), respectively, μ_B is the Bohr magneton, and $\lambda^{\mathrm{Er}} = 0.07$ meV, $\lambda^{\mathrm{Dy}} = 0.2621$ meV and $\lambda^{\mathrm{Er,Dy}} = 0.21$ meV are the exchange parameters for the Er–Er, Dy–Dy and Er–Dy interactions, respectively [33]. The $\mathcal{H}^{\mathrm{Er,Dy}}_{\mathrm{CEF}}$ terms represent the crystalline electrical field (CEF) Hamiltonian for a cubic symmetry in Lea, Leask, and Wolf (LLW) notation [41,42]. Using cubic symmetry for the low-temperature structures is a valid approximation considering that the studied samples, as shown experimentally below, either develop only minor lattice distortions or do not exhibit measurable distortions at all. The CEF parameters used for each rare-earth sublattice are: (i) Er sublattice: $F_4 = 60, F_6 = 13,860$, $X = -0.2620$ and $W = -0.0252$ meV; (ii) Dy sublattice: $F_4 = 60, F_6 = 13,860$, $X = 0.3$ and $W = -0.011$ meV (taken from [10,33]). The F_4 and F_6 parameters depend only on J and are, therefore, identical for Er and Dy.

The eigenvalues (ε_n) and eigenvectors ($|\varepsilon_n\rangle$) of the Hamiltonians (1) and (2) are evaluated through a self-consistent procedure to obtain the magnetization components, M^{R}_i ($i = x, y, z$ and R = Er, Dy), of each sublattice, given by:

$$M^{\mathrm{R}}_i = g^{\mathrm{R}}\mu_B\frac{\sum_n\langle\varepsilon^{\mathrm{R}}_n|J^{\mathrm{R}}_i|\varepsilon^{\mathrm{R}}_n\rangle e^{(-\beta\varepsilon^{\mathrm{R}}_n)}}{\sum_n e^{(-\beta\varepsilon^{\mathrm{R}}_n)}}, \quad (3)$$

where $\beta = 1/k_BT$ and k_B is the Boltzmann constant.

Taking the crystallographic z-axis as a reference, the angle (φ^R) between the magnetic moments and principal crystallographic axes can then be calculated from the magnetization components (3) using the following equation:

$$\varphi^R(\mathrm{T}) = \tan^{-1}\left[\frac{\sqrt{\left(\mathrm{M^R_x}\right)^2 + \left(\mathrm{M^R_y}\right)^2}}{\mathrm{M^R_z}}\right] \quad (4)$$

The magnetic entropy (S_{mag}) is given by:

$$S^R_{mag} = \mathcal{R}\left[\ln\sum_i e^{-\beta\varepsilon^R_i} + \beta\frac{\sum_i \varepsilon^R_i e^{-\beta\varepsilon^R_i}}{\sum_i e^{-\beta\varepsilon^R_i}}\right], \quad (5)$$

where $\mathcal{R}$ is the gas constant. The magnetic heat capacity is then calculated as $C = T\left(\frac{\partial S}{\partial T}\right)$. The lattice vibrational (Debye model approximation) and electronic contributions to total heat capacity are given by:

$$C_{lattice} = 9\,\mathcal{R}\left(\frac{T}{\Theta_D}\right)^3 \int_0^{\theta_D/T} \frac{x^4 e^x}{(e^x-1)^2} dx, \quad (6)$$

$$C_{el}(T) = \gamma T, \quad (7)$$

where $\Theta_D(x,T)$ and $\gamma(x)$ are Debye temperature and Sommerfeld coefficient, respectively. They were calculated considering the relative position of a rare-earth element in the lanthanides series $(\Theta_D,\gamma)^{RAl_2} = \frac{(14-n)(\Theta_D,\gamma)^{LaAl_2} + n\cdot(\Theta_D,\gamma)^{LuAl_2}}{14}$ and the concentration of each sublattice $(\Theta_D,\gamma)^x = (x)(\Theta_D,\gamma)^{ErAl_2} + (1-x)(\Theta_D,\gamma)^{DyAl_2}$ [43]. The coefficients γ^{LaAl_2}, γ^{LuAl_2} $\Theta_D^{LaAl_2}$ and $\Theta_D^{LuAl_2}$ were taken from the literature [43,44].

4. Results

The $Er_{1-x}Dy_xAl_2$ compounds form a continuous solid solution at room temperature, adopting cubic $MgCu_2$ structure type in the paramagnetic state [32]. Close examination of Bragg peaks in the range of $2\theta \geq 50°$ (Mo Kα radiation) confirms that all of the examined samples, including binaries reported in earlier studies (x = 0, 1) [23,24], are cubic (as follows from the absence of splitting) and isostructural at room temperature (Figure 1a). The lattice parameters at 295 K shown in Table 1 confirm the lattice contraction when Er substitutes Dy.

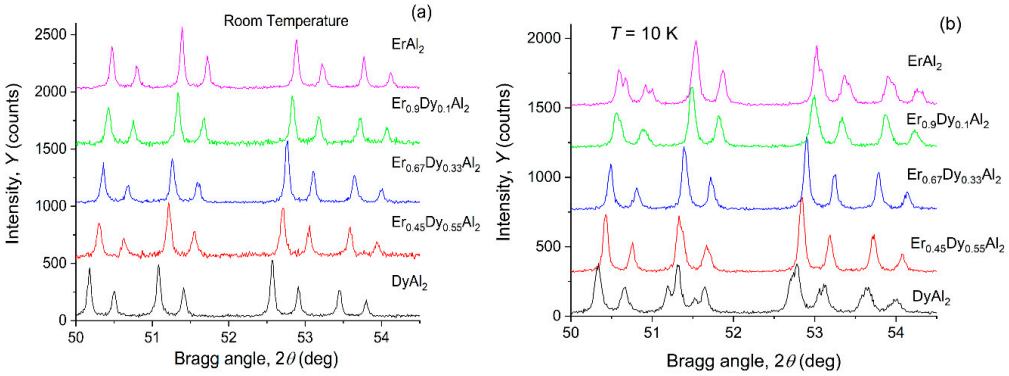

Figure 1. The X-ray powder diffraction patterns (Mo Kα radiation) of $Er_xDy_{1-x}Al_2$ with x = 0, 0.45, 0.67, 0.9, and 1.0 (shown in the range $50 \leq 2\theta \leq 54.5°$ for clarity) measured at room temperature (**a**) and at 10 K (**b**).

Table 1. Critical temperatures of the heat capacity anomalies [31] and crystallographic parameters of the $Er_xDy_{1-x}Al_2$ compounds with x = 0.45, 0.67, and 0.90. T * is the temperature of the second anomaly observed in the heat capacity data.

x (Er)	T_C, K	T *, K	T = 295 K			T = 10 K			
			Space Group	a (Å)	V (Å^3)	Space Group	a (Å)	c (Å)	V (Å^3)
0.45	40	7	$Fd\bar{3}m$	7.8263(1)	479.37(1)	$I4_1/amd$	5.5231(1)	7.8026(2)	238.095(6)
0.67	28	8	$Fd\bar{3}m$	7.8196(1)	478.14(1)	$Fd\bar{3}m$	7.8016(1)	7.8016(1)	474.85(1)
0.90	17	12	$Fd\bar{3}m$	7.8092(1)	476.24(1)	$R\bar{3}m$	5.5082(1)	13.4795(4)	354.19(1)

The compositional dependence of crystal structure is more complex at 10 K as shown in Figure 1b, where PXRD patterns are plotted in the same range of Bragg angles. The splitting of different Bragg peaks seen in the binary compounds, $ErAl_2$ and $DyAl_2$, reflects different structural distortions reported earlier. Mixing Er and Dy markedly suppresses those distortions. Thus, Bragg peaks of $Er_{0.67}Dy_{0.33}Al_2$

do not show visible splitting compared to the room temperature pattern, which is in agreement with our earlier study of the neighboring $Er_{0.75}Dy_{0.25}Al_2$ [30], where the cubic structure is preserved down to 5 K. Close examination of the PXRD patterns of the other two samples, $Er_{0.45}Dy_{0.55}Al_2$ and $Er_{0.9}Dy_{0.1}Al_2$, indicates the possibility of much weaker distortions compared to the binaries, seen as a minor but noticeable broadening of the corresponding Bragg peaks.

It is worth noting that the Rietveld refinement of the low-temperature PXRD patterns of all pseudobinary samples studied here can be performed satisfactorily using the cubic symmetry with only a minuscule increase in residuals. For example, for $x = 0.9$ (Figure 2a), the refinement using the distorted (rhombohedral) structure leads to profile residual, $R_p = 8.4\%$, which is only slightly lower than $R_p = 8.7\%$ for the cubic symmetry (Figure 2b); the Bragg residuals, R_B, are nearly indistinguishable (3.2% vs. 3.1%). Yet, both the visual examination of the Bragg peaks as well as the ability to converge the least-squares refinements using the lower symmetry without imposing constraints on the lattice parameters indicate that the corresponding distortions (rhombohedral for $Er_{0.9}Dy_{0.1}Al_2$ and tetragonal for $Er_{0.45}Dy_{0.55}Al_2$, see Tables 1 and 2) do indeed occur in these samples at low temperatures. On the contrary, the refinements of the room temperature or even 100 K data using non-cubic structural models do not converge without constraining lattice parameters. The data with higher resolution, such as x-ray synchrotron radiation, can examine these distortions with a higher level of accuracy but are unlikely to change the main conclusion of this work, which is the much-suppressed distortions due to Er/Dy substitutions.

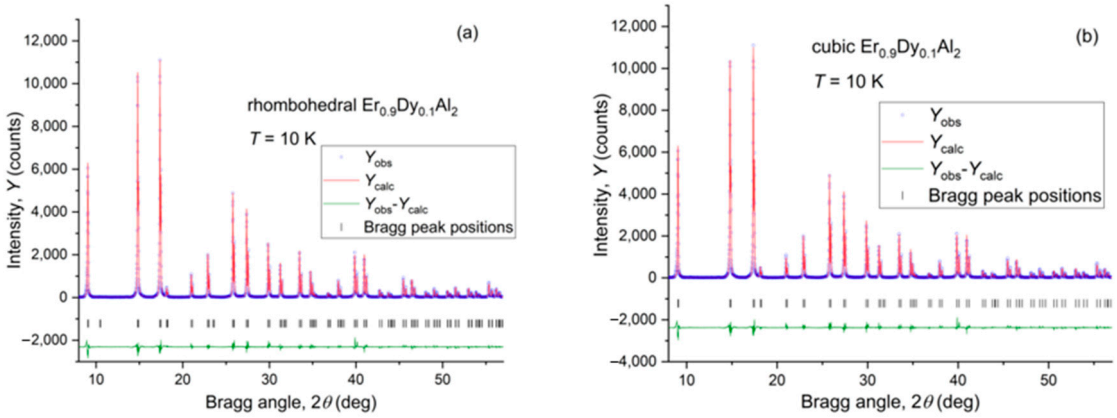

Figure 2. The Rietveld refinements of the powder X-ray diffraction (PXRD) pattern of $Er_{0.9}Dy_{0.1}Al_2$ measured at 10 K using: (**a**) rhombohedral ($R_p = 8.4\%$, $R_B = 3.2\%$) and (**b**) cubic ($R_p = 8.7\%$, $R_B = 3.1\%$) models.

Table 2. Coordinates of atoms in the unit cells of $Er_xDy_{1-x}Al_2$ compounds. The hexagonal setting is adopted for the $R\bar{3}m$ rhombohedral symmetry.

Atom \ Space Group	$Fd\bar{3}m$	$I4_1/amd$	$R\bar{3}m$ h
R(Er+Dy)	1/8, 1/8, 1/8	0, 1/4, 3/8	0, 0, 0.1262
Al1	1/2, 1/2, 1/2	0, 0, 0	0, 0, 1/2
Al2	N/A	N/A	$\frac{1}{2}$, 0, 0

Some of the examined patterns show strong peak shape anisotropy, which, in our opinion, is not purely instrumental and is likely sample-related. Even the use of multi-parameter axial divergence model, employed by FullProf [38,45], did not allow to appropriately treat the low-angle shape anisotropy for $x = 0.45$ and $x = 0.67$ while the peak shape anisotropy of $Er_{0.9}Dy_{0.1}Al_2$ could be accurately refined even by using simple Howard's model [46]. The unaccounted peak shape anisotropy is partially responsible for the elevated values of residuals in the samples with higher Dy content. Additionally, the lack of sample spinning leads to random errors in peak intensities. Below we provide a brief description of the low-temperature structural behavior for each studied sample.

4.1. $Er_{0.9}Dy_{0.1}Al_2$

The $Er_{0.9}Dy_{0.1}Al_2$ (Figure 2) shows the lowest Bragg residuals among the three samples. We note that the sample may be refined using cubic symmetry down to the lowest temperature (5 K), but below ~20 K a rhombohedral distortion (space group $R\bar{3}m$) model provides a stable and reproducible solution indicating that it is likely a stable ground state structure for this sample. The temperature dependence of the lattice parameters (Figure 3) corroborates this suggestion and the degree of the distortion clearly increases on cooling.

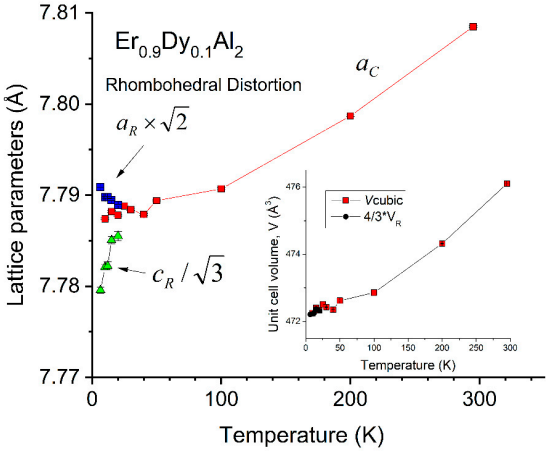

Figure 3. Lattice parameters of $Er_{0.9}Dy_{0.1}Al_2$ as functions of temperature. Inset shows unit cell volume as a function of temperature.

4.2. $Er_{0.45}Dy_{0.55}Al_2$

The low-temperature structural behavior of $Er_{0.45}Dy_{0.55}Al_2$ indicates a very weak tetragonal distortion. The X-ray powder diffraction patterns of this compound may be refined in the cubic symmetry at any temperature, but the refinement shows reproducible convergence using a tetragonal (space group $I4_1/amd$) model below 30 K (Figure 4a). The tetragonal splitting is noticeable at 10 K pattern (right panel of Figure 4b), and the splitting increases with cooling. The low angle asymmetry in the Bragg peaks of this compound significantly affects the quality of the refinement. The temperature dependence of the lattice parameters calculated using the tetragonal model is shown in Figure 5.

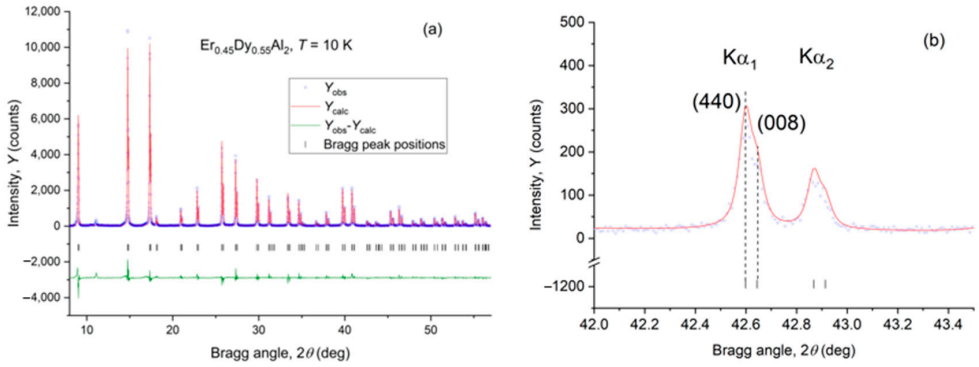

Figure 4. (**a**) The Rietveld refinement of the X-ray powder diffraction pattern of the $Er_{0.45}Dy_{0.55}Al_2$ measured at 10 K using tetragonal model (R_p = 10.7%, R_B = 4.8%). A weak Bragg peak at ~11 deg 2θ is external to the sample (acknowledging that it is impossible to identify a phase from a single Bragg peak, its location coincides with the strongest Bragg peak of the low-temperature cubic ice polymorph [47], and this peak appears below 150 K at low pressures, matching the conditions reported in [47]). (**b**) The tetragonal splitting of the (008) cubic Bragg reflection.

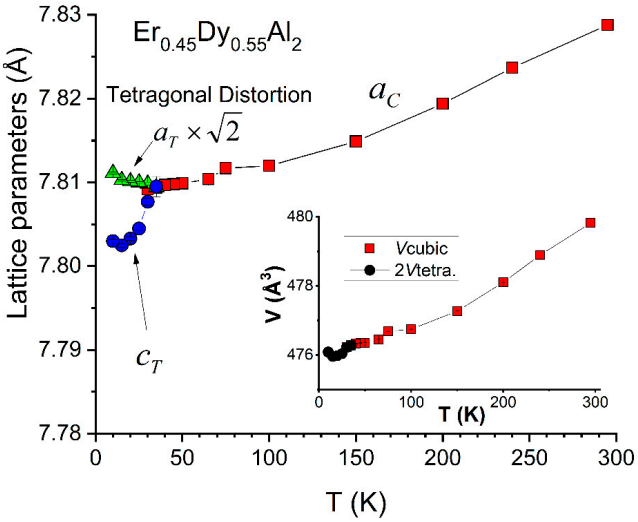

Figure 5. Lattice parameters of $Er_{0.45}Dy_{0.55}Al_2$ as functions of temperature. Inset shows the unit cell volume as a function of temperature.

4.3. $Er_{0.67}Dy_{0.33}Al_2$

The behavior of the $Er_{0.67}Dy_{0.33}Al_2$ sample is nearly identical to that reported for the $Er_{0.75}Dy_{0.25}Al_2$ [30]. No indication of a structural distortion was observed in our measurements (Figures 1 and 6). The lattice parameter *a* steadily decreases on cooling but shows a minor anomaly around T_C ~25 K (Figure 7).

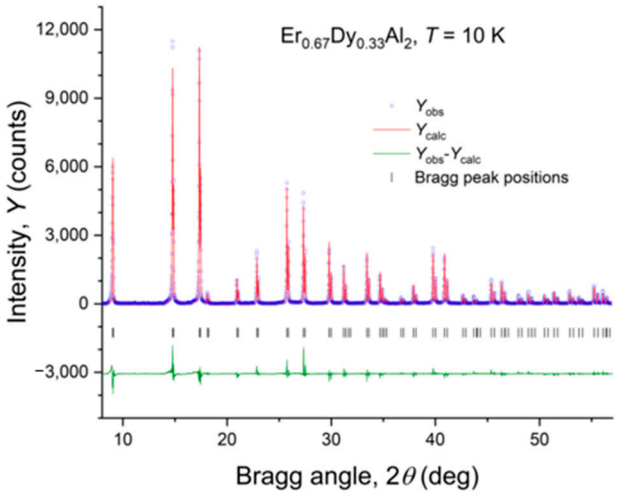

Figure 6. The Rietveld refinement of the X-ray powder diffraction pattern of the $Er_{0.67}Dy_{0.33}Al_2$ measured at 10 K using the cubic model (R_p = 11.3%, R_B = 5.1%).

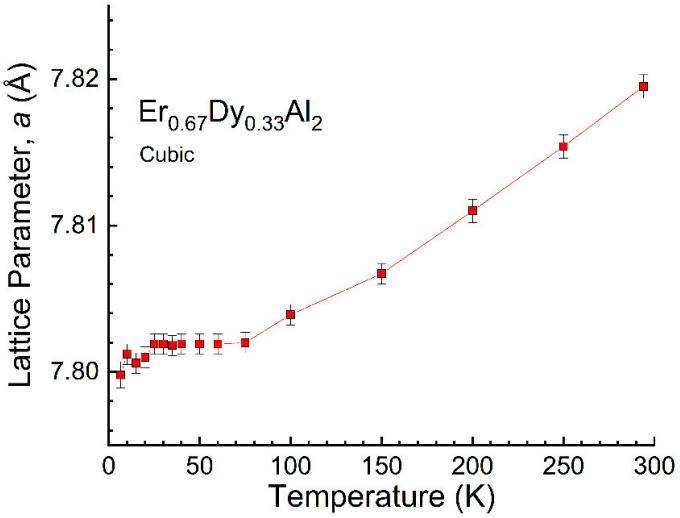

Figure 7. Lattice parameters of the $Er_{0.67}Dy_{0.33}Al_2$ as a function of temperature.

4.4. Easy Magnetization Axis as a Function of Composition

Given the experimentally well-established connection between the EMA and the type of structural distortion, one can reasonably conclude that the structural behaviors observed in this study indicate considerable changes in the magnetic anisotropy of the $Er_xDy_{1-x}Al_2$ compounds with x. However, due to competition between the EMAs of Er and Dy sublattices, there is no longer a clearly defined easy magnetization axis in these alloys. Further, even in the binary $DyAl_2$, the <111> direction is switched to <100> as temperature varies (our calculations do not differentiate between [100], [010], and [001] directions of the cubic lattice). The evolution of the magnetization angle with x (for $0 \leq x \leq 1$), obtained by the mean-field theory analysis, suggests that for low Er concentrations, i.e., when $x <$ 0.47, the easy direction for both sublattices is <100> ($\varphi = 90^{\circ}$) in agreement with the $DyAl_2$ ground state EMA (Figure 8). When x increases, the angle φ decreases for both sublattices changing the easy magnetization direction until the moments align along <111> ($\varphi \approx 54.7^{\circ}$), coinciding with $ErAl_2$ easy direction (Figure 8). Figure 8 shows this behavior for two different temperatures in the ordered region, T = 3 K and 10 K, black and blue curves, respectively. At 3 K, the <100> is the EMA until $x \approx 0.47$, the intermediate state occurs between $0.47 < x < 0.76$, and for $x > 0.76$ the easy magnetization direction is <111>. At 10 K the <100> remains the EMA until $x = 0.7$. However, the transition from the <100> towards the <111> direction happens in a narrower concentration range $0.7 < x < 0.75$. Figure 9 shows φ as a function of temperature for Er (solid lines) and Dy (dashed lines) sublattices calculated for $Er_{0.45}Dy_{0.55}Al_2$ (a), $Er_{0.67}Dy_{0.33}Al_2$ (b) and $Er_{0.90}Dy_{0.10}Al_2$ (c) compounds. For x = 0.45 the EMA is [100] in almost all temperature range, with a minor (~5 deg) deviation below 3 K. For x = 0.67 (transition region in Figure 8) the sublattices are not aligned in the same direction and there is no clear EMA. The lack of well-defined EMA correlates with the presence of heat capacity anomalies when x = 0.67, 0.75, and 0.82 [32]. Our modeling of heat capacity data supports this hypothesis (Figure 10). The discontinuity in the entropy in the magnetically ordered region is observed in x = 0.67 but not in x = 0.45 and 0.90 samples. For x = 0.90 the high Er concentration is responsible for the EMA of the compound to be <111>.

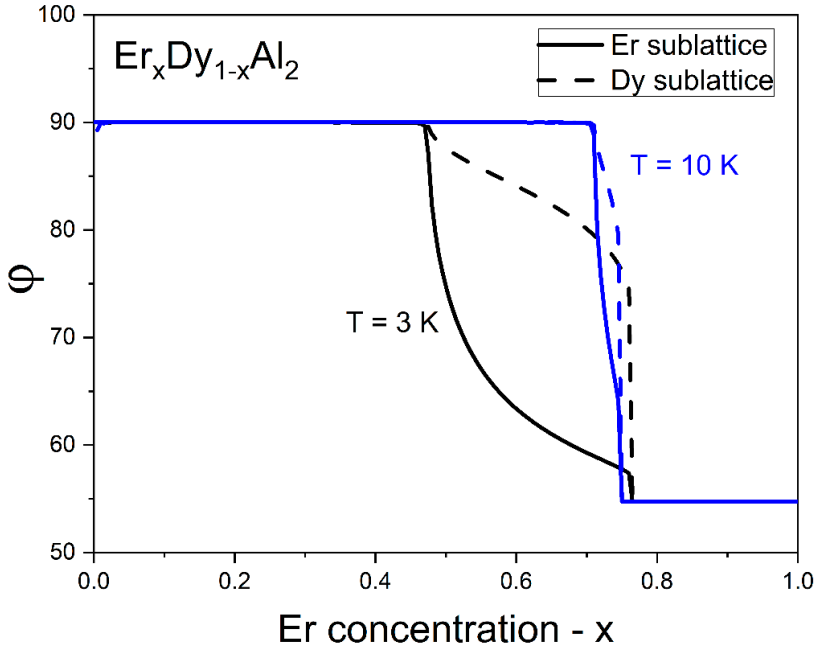

Figure 8. $Er_xDy_{1-x}Al_2$ polar angle (φ) of each magnetic sublattice, Er (solid line) and Dy (dashed), as a function of Er concentration for T = 3 K and 10 K.

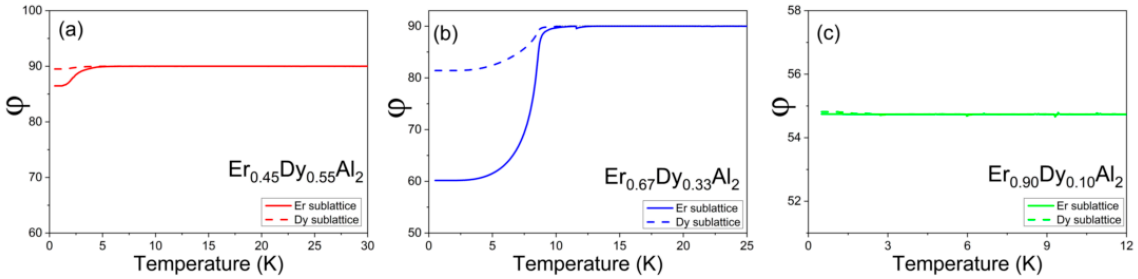

Figure 9. Temperature dependence of the polar angle (φ) of each magnetic sublattice, Er and Dy, for $Er_xDy_{1-x}Al_2$ with x = 0.45 (**a**), 0.67 (**b**), and 0.90 (**c**).

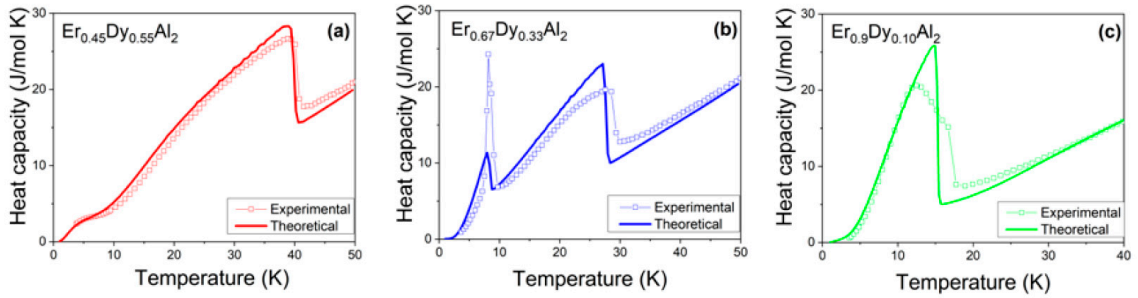

Figure 10. Heat capacity of the $Er_xDy_{1-x}Al_2$ samples with x = 0.45 (**a**), x = 0.67 (**b**), and x = 0.90 (**c**). The symbols are the experimental measurements reported in [32] and the solid lines represent the theoretical results calculated using the model described above.

The calculation results agree well with the XRD data for the x = 0.45 and 0.90 samples since the calculated EMA matches the type of the observed distortion: rhombohedral for <111> and tetragonal for <100>. The calculations also explain the lack of structural distortion when x = 0.67 since there is no clearly established EMA. At the same time, the magnetic moments in both sublattices are mainly oriented in the xy plane for T = 10 K. We speculate that using high-resolution synchrotron X-ray

diffraction one may be able to observe a low-symmetry distortion in the *ab* plane in the $x = 0.67$ (this work) and $x = 0.75$ [30] materials.

5. Conclusions

In the $Er_xDy_{1-x}Al_2$ pseudobinary system the structural distortions, clearly observed in the corresponding binary parents, are strongly suppressed. Minor distortions can be detected in the $x = 0.45$ and 0.9 samples, but at the $x = 0.67$ concentration no evidence of a structural distortion was observed. The experimental results agree with the mean-field theory modeling that confirms the EMA [100] for x = 0.45 and EMA <111> for $x = 0.9$ but indicates the absence of a clearly defined EMA (intermediate state with different orientations of sublattices) for $x = 0.67$. This behavior is contrasting with the structural properties of the $Er_{1-x}Dy_xCo_2$ alloys, where mixing Er and Dy produces clear and strong low-temperature lattice distortions similar to those observed in the $HoCo_2$ compound [3]. Given the limited resolution of laboratory PXRD, we acknowledge that the accuracy of our results may be improved by using the synchrotron radiation, but the conclusions presented here will likely stand.

Author Contributions: Y.M. conceived the study and performed data collection and analyses. B.P.A. and P.O.R. performed modeling and analyzed modeling results. V.K.P. and Y.M. co-supervised research. All authors participated in discussions of the results and partook in writing and revising the manuscript. All authors have read and agreed to the published version of the manuscript.

Funding: This research was funded by the U.S. Department of Energy under contract No. DE-AC-02-07CH11358 with Iowa State University.

Acknowledgments: This work was performed at Ames Laboratory and was supported by the Division of Materials Science and Engineering, Basic Energy Sciences, Office of Science of U.S. Department of Energy (DOE). Ames Laboratory is operated for the U.S. DOE by Iowa State University of Science and Technology under Contract No. DE-AC02-07CH11358. Paula O. Ribeiro and Bruno P. Alho *acknowledge the financial support of* Coordenação de Aperfeiçoamento de Pessoal de Nível Superior—Brasil (CAPES)—Finance Code 001, CNPq—Conselho Nacional de Desenvolvimento Científico e Tecnológico—Brazil and FAPERJ—Fundação de Amparo à Pesquisa do Estado do Rio de Janeiro.

Conflicts of Interest: The authors declare no conflict of interest.

References

1. Gschneidner, K.A., Jr. Systematics of the intra rare-earth binary alloy systems. *J. Less Common Met.* **1985**, *114*, 29–42. [CrossRef]
2. Gschneidner, K.A., Jr. Pressure dependence of the intra rare-earth generalized binary phase-diagram. *J. Less Common Met.* **1985**, *110*, 1–10. [CrossRef]
3. Pathak, A.K.; Paudyal, D.; Mudryk, Y.; Pecharsky, V.K. Role of 4f electrons in crystallographic and magnetic complexity. *Phys. Rev. B* **2017**, *96*, 064412. [CrossRef]
4. Gschneidner, K.A., Jr.; Takeya, H.; Moorman, J.O.; Pecharsky, V.K. $(Dy_{0.5}Er_{0.5})Al_2$-a large magnetocaloric effect material for low-temperature magnetic refrigeration. *Appl. Phys. Lett.* **1994**, *64*, 253–255. [CrossRef]
5. Gschneidner, K.A., Jr.; Pecharsky, V.K. Magnetocaloric materials. *Ann. Rev. Mater. Sci.* **2000**, *30*, 387–429. [CrossRef]
6. Korte, B.J.; Pecharsky, V.K.; Gschneidner, K.A., Jr. The correlation of the magnetic properties and the magnetocaloric effect in $(Gd_{1-x}Er_x)NiAl$ alloys. *J. Appl. Phys.* **1998**, *84*, 5677–5685. [CrossRef]
7. De Gennes, P.G. Interactions indirectes entre couches 4f dans les métaux de terres rares. *J. Phys. Radium* **1962**, *23*, 510–521. (In French) [CrossRef]
8. Kittel, C. Indirect Exchange Interaction in Metals—A Status Report. *J. Appl. Phys.* **1968**, *39*, 637–641. [CrossRef]
9. Levy, P.M. Indirect Exchange in the Rare-Earth Intermetallics. *J. Appl. Phys.* **1970**, *41*, 902–904. [CrossRef]
10. Purwins, H.G.; Leson, A. Magnetic properties of (Rare Earth)Al_2 intermetallic compounds. *Adv. Phys.* **1990**, *39*, 309–403. [CrossRef]
11. Hughes, I.D.; Dane, M.; Ernst, A.; Hergert, W.; Luders, M.; Poulter, J.; Staunton, J.B.; Svane, A.; Szotek, Z.; Temmerman, W.M. Lanthanide contraction and magnetism in the heavy rare earth elements. *Nature* **2007**, *446*, 650–653. [CrossRef] [PubMed]

12. De Gennes, P.G. Helical structures of the heavy rare earth metals. *Solid State Commun.* **1963**, *1*, 62–66. [CrossRef]
13. Andrianov, A.V. Unambiguous dependence of the period of the helicoidal magnetic structure in heavy magnetic rare-earth materials on the ratio c/a of the crystal lattice-possible association with an electron topological transition. *JETP Lett.* **1992**, *55*, 666–669.
14. Von Ranke, P.J.; Alvarenga, T.S.T.; Alho, B.P.; Nobrega, E.P.; Ribeiro, P.O.; Carvalho, A.M.G.; de Sousa, V.S.R.; Caldas, A.; de Oliveira, N.A. Spin reorientation and the magnetocaloric effect in $Ho_yEr_{(1-y)}N$. *J. Appl. Phys.* **2012**, *111*, 113916. [CrossRef]
15. Pecharsky, V.K.; Gschneidner, K.A., Jr. Phase relationships and crystallography in the pseudobinary system Gd_5Si_4-Gd_5Ge_4. *J. Alloy. Compd.* **1997**, *260*, 98–106. [CrossRef]
16. Pecharsky, V.K.; Gschneidner, K.A., Jr. $Gd_5(Si_xGe_{1-x})_4$: An extremum material. *Adv. Mater.* **2001**, *13*, 683–686. [CrossRef]
17. Petit, L.; Paudyal, D.; Mudryk, Y.; Gschneidner, K.A.; Pecharsky, V.K.; Luders, M.; Szotek, Z.; Banerjee, R.; Staunton, J.B. Complex magnetism of lanthanide intermetallics and the role of their valence electrons: Ab initio theory and experiment. *Phys. Rev. Lett.* **2015**, *115*, 207201. [CrossRef]
18. Verhoeven, J.D.; Gibson, E.D.; McMasters, O.D.; Baker, H.H. The growth of single crystal Terfenol-D crystals. *Metall. Mater. Trans. A* **1987**, *18*, 223–231. [CrossRef]
19. Jiles, D.C. The development of highly magnetostrictive rare earth-iron alloys. *J. Phys. D Appl. Phys.* **1994**, *27*, 1–11. [CrossRef]
20. Pecharsky, V.K.; Gschneidner, K.A., Jr. Giant magnetocaloric effect in $Gd_5(Si_2Ge_2)$. *Phys. Rev. Lett.* **1997**, *78*, 4494–4497. [CrossRef]
21. Pecharsky, V.K.; Gschneidner, K.A., Jr. The giant magnetocaloric effect in $Gd_5(Si_xGe_{1-x})_4$ materials for magnetic refrigeration. *Adv. Cryog. Eng.* **1998**, *43*, 1729–1736.
22. Schelp, W.; Drewes, W.; Leson, A.; Purwins, H.G. Low-temperature heat-capacity of some heavy compounds $TbAl_2$, $DyAl_2$, $ErAl_2$, and $TmAl_2$ in a magnetic-field. *J. Phys. Chem. Solids* **1986**, *47*, 855–861. [CrossRef]
23. Khan, M.; Pathak, A.K.; Mudryk, Y.; Gschneidner, K.A., Jr.; Pecharsky, V.K. Anisotropy induced anomalies in $Dy_{1-x}Tb_xAl_2$. *J. Mater. Chem. C* **2017**, *5*, 896–901. [CrossRef]
24. Pathak, A.K.; Paudyal, D.; Mudryk, Y.; Gschneidner, K.A., Jr.; Pecharsky, V.K. Tunable magnetism and structural transformations in mixed light-and heavy-lanthanide dialuminides. *Phys. Rev. B* **2016**, *94*, 224406. [CrossRef]
25. Paudyal, D.; Pecharsky, V.K.; Gschneidner, K.A., Jr. Electronic structure, magnetic properties, and magnetostructural transformations in rare earth dialuminides. *J. Appl. Phys.* **2014**, *115*, 17E127. [CrossRef]
26. Gratz, E.; Markosyan, A.S. Physical properties of RCo_2 Laves phases. *J. Phys. C Condens. Matter* **2001**, *13*, R385–R413. [CrossRef]
27. Duc, N.H.; Hien, T.D.; Givord, D.; Franse, J.J.M.; DeBoer, F.R. Exchange interactions in rare-earth transition-metal compounds. *J. Magn. Magn. Mater.* **1993**, *124*, 305–311. [CrossRef]
28. Khmelevskyi, S.; Mohn, P. The order of the magnetic phase transitions in RCo_2 (R = rare earth) intermetallic compounds. *J. Phys. C Condens. Matter* **2000**, *12*, 9453–9464. [CrossRef]
29. Mudryk, Y.; Paudyal, D.; Pathak, A.K.; Pecharsky, V.K.; Gschneidner, K.A., Jr. Balancing structural distortions via competing 4f and itinerant interactions: A case of polymorphism in magnetocaloric $HoCo_2$. *J. Mater. Chem. C* **2016**, *4*, 4521–4531. [CrossRef]
30. Nirmala, R.; Mudryk, Y.; Pecharsky, V.K.; Gschneidner, K.A., Jr. Unusual magnetism of $Er_{0.75}Dy_{0.25}Al_2$. *Phys. Rev. B* **2007**, *76*, 014407. [CrossRef]
31. Lima, A.L.; Oliveira, I.S.; Gomes, A.M.; von Ranke, P.J. Origin of anomalous magnetocaloric effect in $(Dy_{1-z}Er_z)Al_2$ alloys. *Phys. Rev. B* **2002**, *65*, 172411. [CrossRef]
32. Lima, A.L.; Gschneidner, K.A., Jr.; Pecharsky, V.K.; Pecharsky, A.O. Disappearance and reappearance of magnetic ordering upon lanthanide substitution in $(Er_{1-x}Dy_x)Al_2$. *Phys. Rev. B* **2003**, *68*, 134409. [CrossRef]
33. De Oliveira, N.A.; von Ranke, P.J. Magnetocaloric effect in the Laves phase pseudobinaries $(Dy_{1-c}R_c)Al_2$ (R = Er and Ho). *J Magn. Magn. Mater.* **2008**, *320*, 386–392. [CrossRef]
34. Ribeiro, P.O.; Alho, B.P.; Alvarenga, T.S.T.; Nobrega, E.P.; de Sousa, V.S.R.; Carvalho, A.M.G.; Caldas, A.; de Oliveira, N.A.; von Ranke, P.J. Theoretical investigations on magnetocaloric effect in $Er_{1-y}Tb_yAl_2$ series. *J. Magn. Magn. Mater.* **2015**, *379*, 112–116. [CrossRef]

35. Holm, A.P.; Pecharsky, V.K.; Gschneidner, K.A., Jr.; Rink, R.; Jirmanus, M.N. X-ray powder diffractometer for in situ structural studies in magnetic fields from 0 to 35 kOe between 2.2 and 315 K. *Rev. Sci. Instrum.* **2004**, *75*, 1081–1088. [CrossRef]
36. Hunter, B. Rietica—A visual Rietveld program. International Union of Crystallography Commission on Powder Diffraction Newsletter. 1998. No. 20. Available online: http://rietica.org (accessed on 8 December 2020).
37. Rodriguez-Carvajal, J. Recent advances in magnetic-structure determination by neutron powder diffraction. *Phys. B* **1993**, *192*, 55–69. [CrossRef]
38. Roisnel, T.; Rodriguez-Carvajal, J. WinPLOTR: A Windows tool for powder diffraction pattern analysis. In *Epdic 7: European Powder Diffraction, Pts 1 and 2*; Delhez, R., Mittemeijer, E.J., Eds.; Trans Tech Publications Ltd.: Zurich-Uetikon, Switzerland, 2001; pp. 118–123.
39. De Sousa, V.S.R.; Carvalho, A.M.G.; Plaza, E.J.R.; Alho, B.P.; Tedesco, J.C.G.; Coelho, A.A.; de Oliveira, N.A.; von Ranke, P.J. Investigation on the magnetocaloric effect in (Gd,Pr)Al_2 solid solutions. *J. Magn. Magn. Mater.* **2011**, *323*, 794–798. [CrossRef]
40. Alho, B.P.; Ribeiro, P.O.; Alvarenga, T.S.T.; Carvalho, A.M.G.; von Ranke, P.J. Magnetocaloric effect in $Gd_{(1-y)}Dy_yAl_2$. *Int. J. Refriger.* **2014**, *37*, 297–302. [CrossRef]
41. Lea, K.R.; Leask, M.J.M.; Wolf, W.P. Raising of angular momentum degeneracy of f-electron terms by cubic crystal fields. *J. Phys. Chem. Solids* **1962**, *23*, 1381. [CrossRef]
42. Hutchings, M.T. Point-charge calculations of energy levels of magnetic ions in crystalline electric fields. *Solid State Phys. Adv. Res. Appl.* **1964**, *16*, 227–273.
43. Von Ranke, P.J.; Pecharsky, V.K.; Gschneidner, K.A., Jr. Influence of the crystalline electrical field on the magnetocaloric effect of $DyAl_2$, $ErAl_2$, and $DyNi_2$. *Phys. Rev. B* **1998**, *58*, 12110–12116. [CrossRef]
44. Hill, T.W.; Wallace, W.E.; Craig, R.S.; Inoue, T. Low-temperature heat-capacities and related thermal properties of $TbAl_2$ and $HoAl_2$. *J. Solid State Chem.* **1973**, *8*, 364–367. [CrossRef]
45. Finger, L.W.; Cox, D.E.; Jephcoat, A.P. A correction for powder diffraction peak asymmetry due to axial divergence. *J. Appl. Crystallogr.* **1994**, *27*, 892–900. [CrossRef]
46. Howard, C.J. The approximation of asymmetric neutron powder diffraction peaks by sums of gaussians. *J. Appl. Crystallogr.* **1982**, *15*, 615–620. [CrossRef]
47. Dowell, L.G.; Rinfret, A.P. Low-temperature forms of ice as studied by X-ray diffraction. *Nature* **1960**, *188*, 1144–1148. [CrossRef]